Cascading Degradations Artificially Improving the Lifetime of Li-ion Full Cells using DMC-based Highly Concentrated Electrolyte

Valentin Meunier, F. Capone, R. Dedryvère, A. Grimaud

Cascading degradations artificially improving the lifetime of Li-ion full cells using DMC-based highly concentrated electrolyte

V Meunier, F Capone, R Dedryvère, A Grimaud

Cascading degradations artificially improving the lifetime of Li-ion full cells using DMC-based highly concentrated electrolyte

V. Meunier[1, 5], F. Capone[2, 5], R. Dedryvère[3, 5] and A. Grimaud[1, 4, 5, z]

[1] Chimie du Solide et de l'Energie (CSE), Collège de France, UMR 8260, 75231 Paris Cedex 05, France

[2] Synchrotron SOLEIL, L'Orme des Merisiers, Départementale 128, 91190 Saint-Aubin, France

[3] Institut des Sciences Analytiques et de Physico-Chimie pour l'Environnement et les Matériaux (IPREM - UMR 5254), E2S-UPPA, Université de Pau & Pays Adour, Pau, France

[4] Department of Chemistry, Boston College, Merkert Chemistry Center, 2609 Beacon St., Chestnut Hill, MA, 02467, USA

[5] Réseau sur le Stockage Electrochimique de l'Energie (RS2E), CNRS FR 3459, 80039 Amiens Cedex 1, France

[z] Correspondence: alexis.grimaud@bc.edu

Abstract

The deployment of energy dense Ni-rich NMC ($LiNi_xMn_yCo_zO_2$ with $x > 0.8$) in Li-ion batteries is hampered by a poor interfacial stability above 4.2 V. Among the strategies to mitigate this instability, highly concentrated electrolytes (HCE) has shown a promising resilience at high potential. In this work, we demonstrate that although cells using HCE experience low capacity fading compared to conventional carbonate based-electrolyte, HCE does not prevent oxidation of dimethyl carbonate at high potential. Even worse, this phenomenon cannot be fully offset by lithium intercalation at the negative electrode and eventually leads to lithium plating that precipitates the cell end of life. To circumvent lithium plating, cycling at high temperature is shown to build a more passivating solid electrolyte interphase (SEI); while promising at first, the lithium losses associated with the SEI formation trigger a jump of graphite staging. Only replacing DMC by ethyl carbonate (EC) solvent reduces efficiently the parasitic oxidation and prevents capacity rollover. This work, by the use of adapted testing protocols and analysis workflows, provides the necessary understanding to open new routes for tackling parasitic reaction at high voltage in Li-ion batteries, which including mastering of SEI formation conditions and the use of appropriate solvent.

Introduction

Powered by Li-ion batteries (LIB) which can fulfill criteria regarding autonomy (>300 km/charge), cost (US$ 175 kWh^{-1} at pack level) and lifetime (>1000 cycles, 80% state of charge), electric vehicles are projected to represent more than 60% of sold vehicles by 2030 [1]. To further improve LIB, higher energy densities while alleviating the costs of the used minerals and the associated geopolitical constraints are necessary. The past years have thus seen a regain of interest for developing Ni-rich NMC phases $LiNi_xMn_yCo_zO_2$ ($x + y + z < 1$, $0 < x, y, z < 1$) with $x \geq 0.8$, these materials combining high energy density and avoiding the use of cobalt. However, the voltage at which they must operate to retrieve their theoretical capacity seriously compromises the cell cyclability.

Indeed, above 4.2 V, layered materials experience severe mechanical and chemical degradations. The main culprit of capacity loss was suggested to be the large anisotropic deformation of the lattice [2,3]. Upon cycling, repetitive expansion/shrinkage induces intra- and inter-particles cracking and the electronic disconnection of particles, leading to a loss of active material (LAM) [4]. In addition to the mechanical fatigue, oxygen release at high voltage causes chemical oxidation of the electrolyte and favors the dissolution of the material, both contributing to the densification of the particles' surface which hampers the Li intercalation upon cycling [5]. Not only high voltages trigger the chemical oxidation of the electrolyte, but at voltages above 4.2 V organic carbonate solvents classically employed are electrochemically oxidized [6]. This oxidation can either form a resistive cathode electrolyte interphase (CEI) [6] or release dissolved species in the electrolyte responsible for further side reactions [7,8] such as gases (O_2, CO, CO_2) [9–12] and/or acidic species (H^+). Released species participate in turn to the hydrolysis of PF_6^- anions [8] and favor transition

metal (TM) dissolution [13,14], which, following their migration to the negative electrode, destabilize the solid electrolyte interphase (SEI) [13,15–17] and increase the overall cell impedance [16,18]. Parasitic reactions triggered at high potentials hence accelerate the degradation rate and hinder the cycling of Ni-rich NMCs to their full capacity. Stabilizing the positive interface above 4.2 V is thus of paramount importance to the development of high capacity LIB.

Facing up this challenge, recent years have seen a surge of efforts dedicated to the design and the stabilization of Ni-rich NMC materials using diverse approaches as the doping of active materials [19–21], the design of surface coatings [22–24] or the use of additives for high voltage [25–27]. One strategy recently proposed to tackle instabilities at high potential is the use of so-called highly concentrated electrolytes (HCE) [28]. Thanks to their solvation structure [28], HCE were proposed to circumvent recurrent issues of high-voltages Ni-rich NMC including aluminum corrosion [29,30], dissolution of TM [31] and solvent oxidation [32]. Furthermore, HCE were proposed to form a robust CEI [31]. Owing to these positive attributes, improved capacity retention and cycling rates were reported with Ni-rich materials, albeit using a semi-infinite metallic lithium reservoir as negative electrode [33,34]. Although auspicious breakthroughs have been done in half-cells [35], studies in full cells configuration focusing on long-term aging in practical conditions, including self-discharge and stability tests at high temperatures, are relatively sparse. Furthermore, when performed, no in-depth analysis of lithium inventory or capacity slippages and marching that are necessary to reveal complex phenomena such as shuttling or lithium plating were reported. In other word, despite the promises offered by HCE to stabilize Ni-rich NMC

materials, key knowledge on stability are missing to rationally design and optimize HCE composition for high-voltage applications.

In this work, we subject different HCEs to a benchmark to probe their ability in stabilizing NMC811/graphite cells at high voltage. For that, we used an adapted analysis workflow recently proposed [36] to demonstrate that the high performance of dimethylcarbonate (DMC) -based HCE rely on the sacrificial oxidation of the electrolyte, counter-balanced by plating on the surface of graphite negative electrode. These combined effects artificially sustain high lithium inventory upon aging. Our work unambiguously shows that the positive attribute of DMC-based HCE relies on its ability to achieve high coulombic efficiency for lithium plating/striping, thus delaying the capacity rollover and the cell death. To prevent such phenomenon, we demonstrate how the SEI and the CEI ability to prevent lithium plating and DMC oxidation, respectively, can be enhanced by modulating the temperature during the formation cycles. Finally, we demonstrate that the design of alternative DMC-free HCEs can suppress the electrolyte oxidation at high potential, paving the way towards the development of HCE with true ability to operate at high voltages.

Experimental

Electrode material – Graphite electrodes coated on copper foil with a loading of 1.1 $mAh.cm^{-2}$ were obtained from Cidetec (Spain) and NMC811 coated on aluminum foil with a loading of 1.0 $mAh.cm^{-2}$ from Umicore (Belgium). Graphite electrode were made of 94wt% 15-4 Graphite (Imerys), 2wt% C45 carbon black (Imerys) and a blend of 2wt% styrene butadiene rubber (SBR) BM451B (Zeon) with 2wt% of carboxymethylcellulose (CMC) CRT2000 (DOW chemical) as binders. NMC811 electrodes were made of 95wt% NMC811 (Umicore), 3wt% C65 carbon black and 2wt% polyvinylidene fluoride (PVDF). Electrodes were punched into circular disks of Ø14 mm (positive) and Ø15 mm (negative), giving a capacity balancing N/P = 1.27. Before coin cell assembly, electrodes were dried overnight at 80 °C under reduced pressure.

Coin cell assembly — **2032-type** coin cells, 316-stainless steel grade, were assembled using 1.23 mm thick wave springs and a set of 0.5 and 1 mm spacers (AOT Battery, China). All cells were assembled in an Ar-filled glovebox. Aluminum foils of Ø20 mm were added between the positive electrode and the spacer, and between the spacer and the positive cap to prevent from stainless steel corrosion. A coated polypropylene separator film was used to increase the wettability of the highly concentrated electrolytes (Celgard 3501). Disks were punched and dried at 55°C for ~72 h before use and added as a single layer separator. The electrolyte volume was defined to fill 4-time the total porosity of the separator and both electrodes, i.e. 31.2 µL, and was added in two steps: 15.6 µL on the anode and the remaining 15.6 µL on the separator. Electrolytes used in this study were LP57 VC (1M LiPF6 in EC: EMC 30:70%wt + 2wt% VC, E-lyte, Germany) and LiFSI 5M

in DMC (Solvionic, France). LiFSI 5M EC was made by dissolving the LiFSI salt (99.9% pure, Solvionic, France) into EC (DodoChem, China) at 55°C under vigorous stirring.

Electrochemical tests – Cells were cycled in a controlled temperature chamber (Memmert, Germany) with a BCS-810 potentiostat (BioLogic, France). Before the first charge, cells were rested for 12 h at 55°C. This step aimed to decrease the viscosity of the electrolyte and ensure proper filling of the electrode/separator pores. It was particularly necessary due to the high viscosity of LiFSI 5M DMC, of 120 mPa.s, compared to 2.8 mPa.s for LP57 [28,37].The cell was then equilibrated at room temperature before use. The C-rate is defined from the theoretical capacity of NMC811 (C = 275 $mAh.g^{-1}$) and all capacities were normalized by the active mass material of NMC811. The cycling procedure alternates between 100 cycles at CCCV 1C, i < C/20 and control cycles composed of C/10, i < C/20 + C/20 to assess cell performance. All cells are cycled in voltage range 2.5 – 4.3 V. The first C/10 cycle before the control cycle performed at C/20 allows to reset the lithium inventory in the electrodes that can be underestimated when the last discharge at high current (1C) is followed by low charge current (C/20), as previously observed [38]. The C/20 cycle is thus more representative of the cell performance.

Incremental capacity and derivative voltage analysis – DVA and ICA were performed on cycles recorded at C/20 in a temperature-controlled chamber to ensure conditions close to thermodynamic equilibrium. During ICA, capacity was normalized by active mass material of positive electrode, and dQ/dV curves thus obtained smoothed using binomial filter. For DVA, dV/dQ discharge curves were plotted and fitted using VAWQuum v1.2 freeware provided by the Department of Physics and Atmospheric Science, Dalhousie University, Canada. The references curves, i.e. NMC811 vs Li^+/Li and graphite vs Li^+/Li,

were recorded at C/20 and at the same working temperature as for full cells. Before fitting, the reference and full cell files were reduced to 100 points using linear interpolation and discharge endpoints set to 0 mAh to meet software requirements. The fitting model is:

$$\frac{dV}{dQ}^{model}_{full\ cell} = \left(mass_{pos.} * \frac{dV}{dQ}_{pos.\ vs\ Li} + S_{pos.}\right) - \left(mass_{neg.} * \frac{dV}{dQ}_{neg.\ vs.\ Li} + S_{neg.}\right)$$

with $mass_{pos.}$ & $mass_{neg.}$ (g) the masses of active material for the positive and the negative electrodes, respectively. $S_{pos.}$ & $S_{neg.}$ (mAh) are the relative capacity slippages of the positive and the negative electrodes, respectively. The full cell model was fitted with recorded data by varying masses and capacity slippages of reference curves. The potential of the negative and the positive electrodes are plotted as function of capacity after the fitting.

Study of transition metal dissolution – Solubility tests of transition metals were conducted under Argon atmosphere and consisted in adding ~5 g of anhydrous $NiCl_2$, $MnCl_2$ or $CoCl_2$ (Alfa-Aesar, 99+% purity) in 1.000 mL of LiFSI in DMC electrolyte. Chloride salts have been used in place of TFSI-ones as they show lower solubility; saturation is thus obtained using 1.000 mL. Solutions were vigorously stirred for 3-days at room temperature to reach the thermodynamic equilibrium. The supernatant was recovered after 10 min of centrifugation at 6000 rpm and was further diluted with a HNO_3 2wt% solution (Suprapur, 65% HNO_3, Merck, Ni impurities ≤ 5.0 ppb; Mn, Ni impurities ≤ 0.5 ppb) for ICP-MS analysis.

The migration of transition metals from the NMC811 electrodes was studied by retrieving the graphite electrodes from graphite/NMC811 coin cells cycled 500 cycles at 4.3 V. Graphite electrodes were rinsed with few drops of DMC (~1mL) back and forth and

digested into 10.000 mL of 2wt% nitric acid (Suprapur, 65% HNO3, Merck, Ni & Al impurities ≤ 5.0 ppb; Mn, Co, Li impurities ≤ 0.5 ppb). Solutions were sonicated and let at rest overnight. Solutions were thereafter recovered, centrifuged for 10 min at 6000 rpm and the supernatant filtrated with polypropylene 0.2 µm PP syringe filters. Filtrate was further diluted with a HNO_3 2wt% solution to reach metal concentrations between 1 ppb and 1 ppm (wt ppb & ppm).

The inductive coupled plasma mass spectroscopy (ICP-MS) – Lithium, nickel, manganease and cobalt amounts were quantified with Nexion 2000 ICP–MS (PerkinElmer) after the calibration line was obtained with ten standard points from multi-element standard solution (Certified reference materials in 2% HNO_3, CPA Chem, Bulgaria). Error bars on data plots were obtained from duplicata of a same condition.

In situ UV-visible – Graphite and NMC811 slurries (90% active material) were casted on 316-stainless grids and dried under vaccum at 80°C overnight. The electrodes as obtained were then cycled using ~3 mL of LiFSI 5M DMC in a commercial UV-visible cell (Sphere-energy, France). Voltage scan in the range of 2.5 – 4.3 V was performed at 0.5 mV/s and *ex-situ* UV-visible spectra were recorded with a UV5 Bio spectrometer (Mettler Toledo). The blank spectra was performed beforehand with a prisitine LiFSI 5M in DMC electrolyte.

X-ray photoemission spectrocopy (XPS) – XPS data were collected at GALAXIES beamline of the SOLEIL synchrotron in France [39] using two different photon energies in the hard X-rays range, technique also called Hard X-ray photoemission spectrocopy (HAXPES). The electrochemical cells were opened in a glovebox filled with Ar with O_2 and H_2O contents below 0.1 ppm. The electrodes were soaked in three successive DMC baths (1 min each) to remove the electrolyte from the surface to uncover the SEI. After drying

the electrodes under vaccuum, they were placed onto a sample holder. A vacuum chamber was then used to transfer the sample holder from the argon glovebox to the HAXPES introduction chamber in order to avoid any contact with air. Photon energies of $h\nu$ = 3.0 and 6.9 keV were obtained from the first and the third order reflections of the Si(111) double-crystal monochromator, respectively. The probing depth is defined as three times the photoelectron inelastic mean free path (IMFP) and was estimated from the TPP-2M model developed by Tanuma et al. [40], which uses the density and the band gap of the probed material. It is difficult to estimate accurately the probing depth of the SEI due to its complex chemical composition and morphology. Therefore, a rough estimation was done considering that the SEI is a mixture of carbonaceous and inorganic species, which was approximated as a mixture of Li_2CO_3 and LiF. The density of Li_2CO_3 is 2.1 and its band gap was fixed to 5 eV (with a poor influence on the result), while the density of LiF is 2.6 and its band gap was fixed to 14 eV. The photoelectrons were collected and analyzed by a SCIENTA EW4000 spectrometer, and the energy resolution obtained from the Au Fermi edge was 0.32 eV for 3.0 keV and 0.14 eV for 6.9 keV. The analysis chamber pressure was always kept at around 10^{-8} mbar during the whole experiment, and no charge neutralizer was used. The binding energy scale was calibrated using the C 1s contribution of hydrocarbon at 285 eV. Filters were used to minimize the synchrotron brilliance onto the samples and thus possible degradation of the fragile SEI under the X-ray beam: 95% filter (5% transmittance) at 3.0 keV and 60% filter (40% transmittance) at 6.9 keV.

Results and discussion

To investigate the stability of Ni-rich materials, graphite/NMC811 cells were cycled at 25°C – 4.3 V with conventional LP57 (ethylene carbonate EC: dimethyl ethyl carbonate EMC 1:1 with 1 M $LiPF_6$), LP57 VC (LP57 + 2w% vinylene carbonate) and HCE-DMC (5 M LiFSI in DMC) electrolytes. The cycling procedure is composed of 100 cycles at 1C (CC; CV i < C/20) separated by control cycles at C/20 from which in-depth electrochemical analysis are carried out. Control cycles are referred to as follow: control N is associated to cycle at C/20 recorded after the Nx100 aging cycles at 1C. For instance, control 0 corresponds to the first C/20 cycle carried out before the first 1C aging cycles, while control 2 corresponds to the C/20 performed after 200 aging cycles at 1C. The resulting capacity retentions are plotted in Figure 1a. While the LP57 cell reaches 80% of initial state of charge (SOC) after the 65^{th} cycle (grey), LP57 VC (green) reaches a comparable end-of-life criteria after 130^{th} cycles, confirming that the addition of VC is beneficial for stabilizing the cell at 4.3 V. Through the rest of the study, LP57 VC is thus used as reference electrolyte. When using HCE-DMC (orange), the cell reaches 70% of the initial capacity after 500 cycles, the best performance among the tested electrolytes. However, when looking at the coulombic efficiency (CE), the HCE-DMC cell shows a break: first a sharp increase is recorded until the 90^{th} cycle follows by a drastic drop starting at cycle 250. This observation suggests that despite the good capacity retention, the use of HCE-DMC electrolyte does not completely eliminate all parasitic reactions. To understand the origin of this enhanced capacity retention but diminished CE in HCE-DMC, quantifications of dissolved transition metal and XRD analysis were carried out in the following.

To probe the influence of concentration on the TM dissolution, solubility tests were first carried out for nickel, manganese or cobalt chloride salts ($TMCl_2$ - TM = Ni^{2+}, Mn^{2+} or Co^{2+}) in DMC-based electrolytes. For different LiFSI concentrations ranging from 0 to 5 M, solutions were saturated with $TMCl_2$ salts and vigorously stirred for 48h under inert atmosphere (Argon). After reaching the thermodynamic equilibrium at ambient temperature, the solutions were centrifuged, filtrated, and the TM concentrations were quantified by ICP-MS (Figure 1b). The resulting solubility shows a bell-shape as a function of the salt concentration, with a maximum at 1 M LiFSI. The highest amounts are measured for manganese, followed by cobalt then nickel, this trend remaining mainly the same in the whole range of LiFSI concentration. In diluted regime (< 1 M), increasing the FSI^- concentration enhances the solubility of TM following the formation of $[TMFSI_y]$ complexes, as recently demonstrated [41]. Instead, above 1 M, the weak dissociation of LiFSI salt and the increased activity coefficient for soluble species lower the solubility of $[TMFSI_y]$ complex [41]. As a result, the solubility of metal salts above 1 M of LiFSI abruptly decreases and is measured five-time lower at 5 M compared to that at 1 M [42]. However, the super concentration does not fully eliminate the dissolution of transition metals, suggesting that the positive attributes of HCE-DMC regarding capacity retention are not arising from a decreased dissolution of TMs.

To confirm that the metal dissolution from NMC811 is not at the origin for the better capacity retention, TMs deposited at the graphite negative electrode were quantified after 500 cycles. Graphite electrodes were retrieved after cycling, rinsed with DMC (few drops) and digested into 2wt% nitric acid solutions before TMs to be quantified by ICP-MS (Figure 1c). About 75 µg of metals per cm^2 were measured for both LP57 VC and HCE-DMC

electrolytes, confirming that metals dissolve from NMC811 and incorporate into the SEI upon cycling. To no surprise, nickel is found in large quantity at the anode, followed by manganese and cobalt. However, the amount of Mn is found much greater than the initial stoichiometry, consistent with the greater solubility recorded for manganese salt in Figure 1b and previously observed in the literature [43]. More importantly, the quantity of TMs does not drastically differ between HCE-DMC and LP57 VC electrolytes, indicating that the different TMs lead to the same level of graphite poisoning. This observation suggests that the dissolution and incorporation follow the applied voltage rather than the solubility limit of NMC materials. Furthermore, our results indicate that the solvation structure of HCE does not inhibit the crossover of TMs.

To assess the effect of bulk degradation on capacity fading, X-ray diffraction measurements were carried out for NMC811 electrodes in a discharge state after 500 cycles (Figure 1d). No extra peaks associated with the formation of secondary phases, nor a decrease of peak intensities that would suggest an early fatigue of bulk material was observed. Furthermore, the NMC811 electrode recovered in a discharged state after cycling in HCE-DMC electrolyte shows similar peak position for the (003) diffraction peak at low angle, suggesting a full degree of lithiation at the end of discharge. In contrary, a lowering of the angle for the (003) peak is observed for NMC811 after discharge in LP57 VC electrolyte, indicating of lower lithiation content when compared to the pristine state. This discrepancy in lithiation state can be explained by the low polarization observed when cycling in HCE-DMC compared to LP57 VC (Figure S1), as well as the particle fracture of NMC811 that prevents the full reintercalation of lithium during the discharge. Overall, there is no clear evidence of structural/chemical degradations of bulk material or different

poisoning of the SEI by transition metal dissolution with HCE-DMC that could explain the better capacity retention or the lower CE observed in Figure 1. Rather, interfacial instability, which origins are investigated below, may explain this difference.

Relative slippages of capacity associated with parasitic reactions at the positive and the negative electrodes are retrieved using derivative voltage analysis (DVA) [44] (Figure 2a). When using LP57 VC (lower panel of Figure 2a), the graphite curve shifts to the left (black arrow), indicating that some lithium remains in the negative electrode at the end of the discharge [45]. This observation can be rationalized by degradations at the positive electrode, with a parasitic oxidation inducing an extra lithiation of the graphite upon charge. The greater cell polarization recorded with LP57 VC electrolyte can also explain this phenomenon (Figure S1), hampering the lithium re-insertion in NMC811 upon discharge and leading to the presence of residual lithium in the graphite electrode. Degradations are found similar with HCE-DMC when compared to LP57 VC up to the 2nd control cycle (i.e. 205th cycle, upper panel, 1^{rst} step associated to the blue arrow), which fit is showed in Figure S7. However, after the second control cycle, the graphite curve suddenly shifts back to the right while the NMC811 curve shifts to the left (grey arrow, 2nd step), which triggers the drop of CE recorded in Figure 1a. This observation indicates that the NMC811 electrode becomes gradually more deficient in lithium at the end of each discharge when using HCE-DMC. Moreover, the loss of active material at the negative electrode (LAM $_{NE}$) reaches 33% of its initial mass suggesting a loss of electrical contact between particles, pores clogging or electrode delamination [46,47]. Altogether, the analysis of the electrochemical cycling data reveals that an increase in degradations at the negative electrode from the 200th cycle onwards is at the origin for the loss of lithium

inventory (LLI) [36], which is the main contribution to cell capacity loss (Figure S8b). Cells cycled using HCE-DMC electrolyte are thus plagued by significant degradations at both interfaces, alike in LP57 VC electrolyte, with nonetheless a different origin.

To complete our understanding of interfacial degradations occurring in HCE, the capacity shift of the charge (Q_C) and discharge (Q_D) endpoints are plotted in cumulative capacity as a function of cycle numbers (Figure 2b). For LP57 VC electrolyte (green), Q_D endpoints increase due to LLI associated with the SEI growth, as previously revealed by DVA [48]. Instead, the relative stability of Q_C advocates for the absence of electrolyte oxidation. Hence, the capacity loss can be ascribed, in addition to the rise in cell polarization, to side reactions at the negative electrode that gradually closes the cycling window (i.e. $Q_C - Q_D$). For the HCE-DMC electrolyte (orange), Q_C quickly increases confirming the parasitic oxidation previously revealed by the DVA (Figure 2a). A poor passivation of the aluminum can be discarded as the origin for the parasitic oxidation, as linear sweep voltammetry recorded on aluminum current collector shows no dramatic oxidation (Figure S2) and the amount of aluminum found at the graphite electrode is similar between HCE-DMC and LP57 VC electrolytes (Figure 1c). Instead, electrolyte components are likely oxidized, increasing the lithiation degree of the graphite electrode beyond that matching the lithium de-intercalation from NMC811. From the 250th cycle onwards (grey part, 2nd step), a rollover is observed for Q_D endpoints, indicating the destabilization of the negative interface.

The conclusion is therefore twofold. First, degradations recorded with LP57 VC electrolyte are mainly caused by the SEI growth and the increased polarization. Second, cells cycled in HCE-DMC electrolyte are plagued by a parasitic oxidation that artificially and

temporarily sustains high capacity retention; beyond the 250th cycle the negative interface becomes unstable and the performance very rapidly decays.

The parasitic oxidation in HCE-DMC was further investigated by self-discharge tests (Figure 2c). In LP57 VC electrolyte, a very limited voltage drop (-0.03 V) is observed after 50 h at open circuit voltage at both 3.8 V or 4.3 V, suggesting a relatively good stability of the electrolyte in this potential range or an enhanced passivation of the interfaces. While similar voltage loss is obtained at 3.8 V for HCE-DMC, the cell experiences a significant drop of -0.13 V at 4.3 V after 50 h, suggesting a spontaneous re-lithiation of NMC811 likely associated with the oxidation of the electrolyte. While parasitic reactions at the graphite electrode cannot be discarded, the absence of self-discharge at 3.8 V strongly suggests that it is not responsible for the rapid voltage decay recorded after charging at 4.3 V. Instead, the self-discharge recorded for HCE-DMC suggests that the electrochemical oxidation of the electrolyte occurs, even if not contributing much to the capacity loss [8,11]. Indeed, the rate loss of -2.6 mV/h (-0.13 V / 50h) measured at 4.3 V corresponds to a capacity loss of only -0.3 mAh, or a parasitic current of ~6 µA (300 µAh / 50 h).

Similar parasitic anodic currents have been recorded, in particular in DMC-based electrolytes, and were found to induce a coloration of the electrolyte [49]. *In-situ* UV-visible measurements were thus performed (Figure 2d). Upon cycling, colored species appeared at the NMC811 electrode (brown) within a dozen of hours, which migration is slow due to the high viscosity of the electrolyte (see inset in Figure 2d). The recorded UV spectrum shows three absorption bands at 223, 272 and 363 nm, matching those previously reported in 1.5 M $NaPF_6$ DMC electrolyte [49]. Moreover, a similar UV-visible spectrum was

obtained when using stainless steel and lithium electrodes in HCE-DMC (Figure S3), which indicates that the color does not stem from the complexation of any released TM from the NMC electrode. From this measurement, we conclude that DMC is most likely oxidized, which however does not explain the brutal switch of degradation regime initially dominated by the positive electrode at early stage of cycling to degradations at the negative electrode after 200 cycles.

To unveil the origins of the switch in degradation regime observed for HCE-DMC, incremental capacity analysis (ICA) is performed. When using LP57 VC (Figure 2e), the intensity of the peak at 4.11 V ascribed to NMC811 decreases upon cycles, confirming the LAM at the positive electrode (LAM_{PE}) initially observed by DVA (Figure 2a). Moreover, the greater peak splitting observed with cycling reveals a rise of cell impedance [15]. While similar conclusions can be drawn for HCE-DMC (Figure 2f), an additional feature is observed at 4.21 V upon charge (resp. 4.16 V upon discharge), most likely associated to lithium plating (resp. stripping) on graphite surface [46]. The occurrence of Li plating matches with the onset cycle estimated using the capacity marching in charge. In details, considering a N/P balancing ratio of 1.27 and specific capacities of Q positive and Q negative of 1.54 mAh and 1.95 mAh, respectively, a safety capacity margin of 0.41 mAh is estimated. In addition, the progression of the charge capacity endpoint (Qc) is predominantly associated to parasitic oxidation occurring at the positive electrode (as seen in DVA), which average slope is +0.008 mAh per cycle between the 1st and 100th cycle. Consequently, after 51 cycles (0.41 mAh / 0.008 mAh.cycle-1), the parasitic oxidation exceeds the safety margin, leading to Li plating as the graphite electrode reaches its full capacity as observed in control 1 (Figure 1f). In addition, this interpretation

is in agreement with the high LAM recorded at the negative electrode (Figure 2a), as lithium plating was previously shown to lead to pore clogging, electrical insulation of graphite particles or electrode delamination [46,47].

Although Li plating is observed at early stage of cycling, the cell performance are sustained up to the 250th cycle owing the previously reported ability of HCEs to plate/strip lithium with high CE [35,50,51]. This conclusion is consistent with the low LLI and capacity fading observed in Figure 1a. Due to this relatively good CE, 250 cycles are necessary for the LLI associated with lithium plating to be sufficient to trigger the capacity rollover. It is important to note that the quantity of lithium amount in the HCE electrolyte is two times higher than in NMC811, and 5 times greater than that for LP57 electrolytes. This factor potentially delays the appearance of detrimental effects due to lithium plating upon aging. Finally, one must note that no lithium plating is recorded for LP57 VC electrolyte, which would have led to a rapid rollover of capacity fading, as previously observed [52–54].

In conclusion, the degradations observed at the positive and the negative interfaces in cells using HCE-DMC are interconnected. Indeed, DMC solvent is anodically decomposed upon charge, the additional capacity associated with this oxidation cannot be completely compensated by the sole intercalation of Li cation in graphite resulting in Li plating. Up until the 250th cycle, lithium plating cannot be detected by the use of metrics such as capacity retention of CE, and only once the effects have sufficiently accumulate to destabilize the negative electrode a drop in CE and a knee point in the capacity retention curve are observed [53]. To tackle this cascading effect, two strategies are proposed.

First, to alleviate the Li plating issues, cells were cycled at 55°C, temperature at which Li plating reaction is disfavored [54,55]. The capacity retention recorded at 55°C for HCE-DMC

is relatively similar to that recorded at 25°C, albeit the initial capacity that is greater due to the enhance kinetics for intercalation at high temperature. Instead, CE is found steady at 99.7%, unlike at 25°C where a rollover was recorded after 200 cycles (Figure 3a). The DVA (Figure 3b) and the evolution of capacity endpoints (Figure 3c) both show that cycling at elevated temperature is beneficial to reduce the rates of side reactions. In particular, no sign of lithium plating is detected (see the ICA in the inset of Figure 3c), which reduces the LLI associated with parasitic reactions at the negative electrode (Figure 3b). It is worth noting that the peak associated with the NMC811 plateau at 4.2 V is lost after the 5th control, which we assume to be due to an increase in cell impedance (Figure S1). However, at this stage, it remains unclear if the positive effect of temperature is solely associated to the enhanced kinetic of lithium intercalation reducing plating risks and/or to the stabilization of the interphases.

To determine the role of the interphases on the improved performance, the effect of pre-forming each interphase at 55°C was tested independently. For that, the SEI and the CEI were pre-formed at 55°C by cycling cells in HCE-DMC electrolyte at C/20, before being re-assembled with complementary electrodes. In other words, the aged NMC811 and its CEI was paired with a pristine graphite electrode, while the aged graphite and its SEI was paired with a pristine NMC811 electrode. Finally, a third cell in which both the SEI and the CEI were pre-formed at 55°C was prepared. The process is summarized in Figure 4a and the results obtained at 25°C with the newly assembled full cells are shown in Figure 4b and 4c. While the capacity retention is found similar for all three cases (Figure 4b), degradation rates clearly differ (Figure 4c). When the CEI is pre-formed (black cell), the shift of capacity endpoints is similar to that recorded without pre-formation, i.e. +0.045

mAh/cycle (Figure 4c) vs. +0.038 mAh/cycle (Figure 1a), indicating that the sole passivation of the CEI is not sufficient to eliminate the parasitic oxidation. Moreover, the ICA (Figure 4d) shows once again the features previously ascribed to Li plating, alike the cell cycled at 25°C. This observation confirms that the instability caused by Li plating is responsible for the capacity rollover from the 250th cycle onwards (Figure 4b). When the SEI is pre-formed at 55°C (red cell), the rapid shift of capacity endpoints (Figure 4c) is similar to that observed for the cell cycled at 25°C without SEI formation, consistent with a copious electrolyte (DMC) oxidation. However, lithium plating is no longer observed (Figure 4e), suggesting that the preformation of the negative interphase can efficiently reduce the plating and prevent the capacity rollover.

Only pre-forming both the SEI and the CEI at 55°C leads to a significant decrease of the capacity shifting rate, i.e. 0.02 mAh/cycle, associated with a better CE (blue cell). The ICA (Figure 4f) shows a doubling of the peak at 4.11 V with the progressive appearance of a peak at 4.08 V upon successive charges (resp. 4.08 to 4.05 V for discharge). This peak doubling is the result of a graphite staging jump (GSJ) [36,56,57]. Indeed, the copious LLI resulting from the SEI and the CEI formation at 55°C lowers the lithiation degree of the negative electrode at the end of charge. Graphite ends the charge on the stage II of intercalation, at 110 mV, instead of the stage I at 80 mV. Eventually, this 30 mV upshift of graphite operating potential significantly reduces the risk of lithium plating. Altogether, our results suggest that pre-forming the interphases at 55°C influences their chemical nature / stability and conditions the capacity window at which electrodes operate, including GSJ.

To get more insight into the chemical composition of the SEI, XPS experiments were carried out on graphite electrodes recovered after 100 cycles at both 25 and 55°C from

graphite/NMC811 cells cycled using LP57 VC and HCE-DMC electrolytes. For a better understanding of the SEI composition as a function of depth, two different photon energies were used, namely 3.0 and 6.9 keV (hard X-ray range), provided by synchrotron radiation. These two photon energies provide probing depths estimated at 20-25 nm and 40-50 nm, respectively (see experimental details). Independently of the photon energy, the use of Hard X-ray photoemission spectrocopy (HAXPES) allowed reaching a greater probing depth than the SEI thickness, and therefore detecting the C 1s signal of graphite. The results are shown in Figure 5 for 3.0 keV photon energy and in Figure S4 for 6.9 keV.

The C 1s spectra of all samples (Figure 5a) show the same components, *i.e.* a thin and asymmetric component at low binding energy (~283 eV) assigned to graphite and four components at 285 eV, 286.5-287 eV, ~288 eV, and 289.5-290 eV attributed to hydrocarbon (CH_x), one-oxygen, two-oxygen and three-oxygen (carbonate) environments of carbon, respectively. The observed binding energy (B.E.) of graphite is ~1 eV weaker than observed for pure graphite material. This difference cannot be attributed to the lithiation of graphite, but instead to the differential charging effect between the SEI and the graphite substrate during the ejection of photoelectrons due to the great difference of electronic conductivities between them. The four other components are in good agreement with what is classically observed for the SEI obtained with carbonate-based electrolytes, *i.e.* carbonaceous species resulting from the reduction of solvents [58]. Note that a weak additional component at ~291 eV is also observed, which can have two origins, first the polymerization of VC at the surface of graphite leading to poly(VC) in the case of LP57 electrolyte [58], secondly to the π-π^* shake-up satellite of graphite peak. The F 1s spectra (Figure 5b) consists of two components: a first one at high B.E. assigned to

the salt (PF_6^- in the case of LP57 VC, and FSI^- in the case of HCE-DMC), and a second one at lower B.E. (~685 eV) attributed to LiF which is the common degradation compound observed for fluorinated salts. Degradation compounds of the salts are also detected in P 2p spectra (for $LiPF_6$) by the presence of a P 2p doublet at low B.E. (~134 eV) corresponding to phosphates, and in N 1s spectra (for LiFSI) by the presence of a component at low B.E. (~398.5 eV) arising from the break of S−F bonds and subsequent formation of LiF [59].

The O 1s spectra (Figure 5c) are rather different for the two different electrolytes. For LP57 VC, they consist of two components at ~532 and ~533.5 eV which are in good agreement with oxygenated carbonaceous species such as Li_2CO_3 and lithium alkylcarbonates, commonly described as the main species of the SEI [60]. For HCE-DMC, the O 1s spectra are modified by the presence of the oxygenated salt $LiN(SO_2F)_2$. Besides, most of O 1s spectra display at low B.E. (~528 eV) a very weak component corresponding to Li_2O, easily detected as well separated from the other components, but corresponding to a very small amount in the SEI.

Looking at the differences between these samples, an important feature is the relative intensity of the C 1s component of graphite with respect to the other carbonaceous species, this ratio providing a qualitative idea regarding the SEI thickness. For LP57 VC electrolyte, the SEI thickness is much greater after cycling at 55°C than at 25°C (the relative area of C 1s components corresponding to the SEI is indeed multiplied by two with respect to graphite). Even so, the SEI thickness still remains below the probing depth (20-25 nm at 3 keV) since the signal of graphite is clearly detected. Unfortunately, no detailed quantification of species can be given due to the lack of reliable photoionization

cross section database and of the analyzer transmission function at each possible photon energy of the beamline. However, quantitative comparisons between samples can be done. For example, for LP57 VC electrolyte, the F 1s / C 1s area ratio decreases by a negligible amount of 7% from 25°C to 55°C. This indicates that the global amount of fluorinated species is similar at the two temperatures. However, the relative amount of LiF with respect to PF_6^- is much greater at 55°C compared to 25°C, in good agreement with an enhanced degradation of the salt promoted by the temperature. This enhanced salt degradation is also clearly seen in the P 2p spectra showing more phosphates with respect to PF_6^- at 55°C. As a result, we can conclude that the SEI is thicker, and richer in inorganic species originating from the salt degradation at 55°C. This observation should be seen in conjunction with the electrochemical results. Indeed, a similar capacity fading upon cycling is observed at both temperatures for LP57 VC electrolyte. Hence, although the SEI is thicker at 55°C and should therefore correspond to an increase of interfacial impedance, this is counterbalanced by a faster kinetic for lithium exchange. Similar observations can be done for HAXPES spectra recorded with the greater photon energy (6.9 keV, see Figure S4) corresponding to a doubling of the probing depth. The relative area of the C 1s components corresponding to the SEI is indeed doubled compared to graphite, confirming the thickening of the SEI.

Turning then to the HCE-DMC electrolyte, the effect of temperature on the SEI thickness is opposite: the SEI is thinner at 55°C than at 25°C. As seen from the C 1s signal of graphite in Figure 5a, the relative area of C 1s components corresponding to the SEI is divided by 2.4 with respect to graphite. The SEI thickness for HCE-DMC at 25°C is the greatest measured for these two series of samples. In parallel, the F 1s / C 1s area ratio

decreases by 32% at 55°C, indicating that the SEI has been significantly depleted in fluorinated species at 55°C compared to 25°C. These observations are again in good agreement with the electrochemical results. Indeed, lithium plating was observed upon over-lithiation of the graphite electrode taking place at 25°C, which is consistent with a thick and resistive SEI delaying intercalation into graphite. On the contrary, at 55°C the SEI is not only thinner but also contains less inorganic (and supposedly more resistive) species than at 25°C, with a resulting positive effect on the electrochemical performances. The results suggest that lithium plating observed at 25°C with HCE-DMC leads to more electrolyte decomposition at the negative electrode, this result is consistent with the increase of the LLI during DVA (Figure 2a) and the rollover of marching capacity (Figure 2b).

While temperature was shown to prevent lithium plating in HCE-DMC, this does not suppress the chemical origin for this reaction which arises from the parasitic oxidation of DMC. DMC was then replaced by EC to form a LiFSI 5M in EC (HCE-EC) electrolyte which was tested at 25°C and 55°C (Figure 6a). At 25°C, the capacity retention curve shows a single slope degradation and a significantly improved CE of 99.4% in average. The marching of capacity endpoints (Figure 6b) and the DVA (Figure 6c) both show no significant parasitic oxidation when compared to HCE-DMC. The main origin for the capacity loss can thus be attributed to the LLI associated with the growth of the SEI (shift to the left of the positive electrode). This LLI cannot be attributed to higher transition metal amounts, as suggested by ICP-MS quantification in Figure S5. At 55°C, no parasitic oxidation is detected and the faster capacity fading when compared to 25°C is again attributed to the LLI being favored at high temperatures.

Finally, no lithium plating/striping is observed during ICA (Figure 6d) and thus no rollover in the capacity marching plots are observed at 25°C or 55°C. Bearing in mind that lithium plating was demonstrated to be the direct result of the extra capacity arising from DMC oxidation, our results show that the positive attribute of HCE-EC is its stability and lack of parasitic oxidation at high potential. Nevertheless, the DVA shows that HCE-EC suffers from a drastic LLI at the negative electrode and an uncontrolled growth of the SEI when cycled at 55°C.

Conclusion

While cycling NMC811 at high potential (4.3 V) is associated with a rapid capacity decay, our work confirms that, at first glance, the use of HCE-DMC improves the performance of graphite/NMC811 cells. Nevertheless, a careful analysis of the electrochemical results using DVA, ICA and capacity marching reveals that the good performance of HCE-DMC are artificially maintained and that the cell chemistry is plagued by a cascade of side reactions. Triggering this cascade is the anodic decomposition of DMC at high potential which, unlike previously believed, is not prevented by the use of highly concentrated electrolyte. The extra capacity arising from DMC oxidation is counter-balanced by an over-lithiation of the graphite electrode which causes lithium plating. Unlike in diluted carbonate electrolytes for which lithium plating readily leads to a capacity rollover, the high CE associated with lithium plating/striping in HCE does not cause any drop in capacity. Only after 250 cycles the build-up of degradations eventually destabilizes the negative electrode and precipitates the capacity fading.

To circumvent the lithium plating, two strategies are proposed in this work: the design of DMC-free HCE and the mastering of the SEI and CEI stability by the use of pre-formation steps at elevated temperatures. Hence, our work reveals that when cycling at 55°C the SEI is thinner and less resistive, helping to prevent Li plating on the graphite surface. High temperatures conditions also the capacity / voltage windows of electrodes and postpone the occurrence of lithium plating as the result of GSJ and the upshift of working potential at the negative electrode. Furthermore, comparing the results obtained in HCE-DMC and HCE-EC, we confirm the detrimental role played by DMC at high potential where EC-based HCE do not show any sign of parasitic oxidation at 4.3 V and thus no lithium plating

at the negative electrode. However, copious LLI are observed when cycling at 55°C, significantly limiting the capacity retention recorded with HCE-EC. Ultimately, our results indicate that an appropriate choice of solvent can efficiently circumvent a cascade of side reactions upon cell aging. The sole switch to EC solvent has indeed stabilize the positive interface and avoided the rollover failure. Although an instability remains at the negative interface, the use of additives as used for the optimization of dilute electrolytes could potentially alleviate this issue. Finally, only the use of appropriate electrochemical analysis and analysis workflows could reveal such complex phenomena [36], in which side reactions trigger each other', pushing for their widespread adoption in the field to evaluate the benefits associated with any novel electrolyte and avoid any false positive.

Acknowledgments

The authors acknowledge the project BATTERY 2030 funded by the European Union's Horizon 2020 research and innovation programme under Grant Agreement No. 957213. The authors acknowledge the project BIG-MAP funded by the European Union's Horizon 2020 research and innovation programme under Grant Agreement No. 957189. The authors acknowledge the French National Research Agency for its support through the Labex STORE-EX project (ANR-10LABX-76-01).

HAXPES experiments were performed on the GALAXIES beamline at SOLEIL Synchrotron, France, under Proposal No. 99220087. We are grateful to Jean-Pascal Rueff for his assistance during the experiments. The authors gratefully acknowledge F. Dorchies for UV-visible measurements and J. Louis for XRD analysis. The authors thank the Department of Physics and Atmospheric Science, Dalhousie University, Canada, for providing dV/dQ fitting freeware (VAWQuum v1.2).

References

1. *Technology and Innovation Pathways for Zero-carbon-ready Buildings by 2030*, Paris, (2022) https://www.iea.org/reports/technology-and-innovation-pathways-for-zero-carbon-ready-buildings-by-2030.

2. Märker, K., Reeves, P.J., Xu, C., Griffith, K.J., and Grey, C.P. (2019). Evolution of Structure and Lithium Dynamics in LiNi0.8Mn0.1Co0.1O2 (NMC811) Cathodes during Electrochemical Cycling. Chemistry of Materials 31, 2545–2554. 10.1021/acs.chemmater.9b00140.

3. Xu, C., Reeves, P.J., Jacquet, Q., and Grey, C.P. (2021). Phase Behavior during Electrochemical Cycling of Ni-Rich Cathode Materials for Li-Ion Batteries. Advanced Energy Materials 11, 1–12. 10.1002/aenm.202003404.

4. Yoon, C.S., Jun, D.W., Myung, S.T., and Sun, Y.K. (2017). Structural Stability of LiNiO2 Cycled above 4.2 v. ACS Energy Letters 2, 1150–1155. 10.1021/acsenergylett.7b00304.

5. Xu, C., Märker, K., Lee, J., Mahadevegowda, A., Reeves, P.J., Day, S.J., Groh, M.F., Emge, S.P., Ducati, C., Layla Mehdi, B., et al. (2021). Bulk fatigue induced by surface reconstruction in layered Ni-rich cathodes for Li-ion batteries. Nature Materials 20, 84–92. 10.1038/s41563-020-0767-8.

6. Azcarate, I., Yin, W., Méthivier, C., Ribot, F., Laberty-Robert, C., and Grimaud, A. (2020). Assessing the Oxidation Behavior of EC:DMC Based Electrolyte on Non-Catalytically Active Surface. Journal of The Electrochemical Society 167, 080530. 10.1149/1945-7111/ab8f57.

7. Boulanger, T., Eldesoky, A., Buechele, S., Taskovic, T., Azam, S., Aiken, C., Logan, E., and Metzger, M. (2022). Investigation of Redox Shuttle Generation in LFP/Graphite and NMC811/Graphite Cells. Journal of The Electrochemical Society 169, 040518. 10.1149/1945-7111/ac62c6.

8. Rinkel, B.L.D., Hall, D.S., Temprano, I., and Grey, C.P. (2020). Electrolyte oxidation pathways in lithium-ion batteries. Journal of the American Chemical Society 142, 15058–15074. 10.1021/jacs.0c06363.

9. Pritzl, D., Solchenbach, S., Wetjen, M., and Gasteiger, H.A. (2017). Analysis of Vinylene Carbonate (VC) as Additive in Graphite/LiNi 0.5 Mn 1.5 O 4 Cells. Journal of The Electrochemical Society 164, A2625–A2635. 10.1149/2.1441712jes.

10. Jung, R., Metzger, M., Maglia, F., Stinner, C., and Gasteiger, H.A. (2017). Oxygen Release and Its Effect on the Cycling Stability of LiNi x Mn y Co z O 2 (NMC) Cathode Materials for Li-Ion Batteries . Journal of The Electrochemical Society 164, A1361–A1377. 10.1149/2.0021707jes.

11. Jung, R., Metzger, M., Maglia, F., Stinner, C., and Gasteiger, H.A. (2017). Chemical versus electrochemical electrolyte oxidation on NMC111, NMC622, NMC811, LNMO, and conductive carbon. Journal of Physical Chemistry Letters 8, 4820–4825. 10.1021/acs.jpclett.7b01927.

12. Rinkel, B.L.D., Vivek, J.P., Garcia-Araez, N., and Grey, C.P. (2022). Two electrolyte decomposition pathways at nickel-rich cathode surfaces in lithium-ion batteries. Energy and Environmental Science 15, 3416–3438. 10.1039/d1ee04053g.

13. Jung, R., Linsenmann, F., Thomas, R., Wandt, J., Solchenbach, S., Maglia, F., Stinner, C., Tromp, M., and Gasteiger, H.A. (2019). Nickel, Manganese, and Cobalt Dissolution from Ni-Rich NMC and Their Effects on NMC622-Graphite Cells. Journal of The Electrochemical Society 166, A378–A389. 10.1149/2.1151902jes.

14. Gilbert, J.A., Shkrob, I.A., and Abraham, D.P. (2017). Transition Metal Dissolution, Ion Migration, Electrocatalytic Reduction and Capacity Loss in Lithium-Ion Full Cells. Journal of The Electrochemical Society 164, A389–A399. 10.1149/2.1111702jes.

15. Meunier, V., and Grimaud, A. (2022). Electrochemical Protocols to Assess the Effects of Dissolved Transition Metal in Graphite / LiNiO 2 Cells Performance Electrochemical Protocols to Assess the Effects of Dissolved Transition Metal in Graphite / LiNiO 2 Cells Performance. 10.1149/1945-7111/ac7e7a.

16. Joshi, T., Eom, K., Yushin, G., and Fuller, T.F. (2014). Effects of Dissolved Transition Metals on the Electrochemical Performance and SEI Growth in Lithium-Ion Batteries. Journal of The Electrochemical Society 161, A1915–A1921. 10.1149/2.0861412jes.

17. Solchenbach, S., Hong, G., Freiberg, A.T.S., Jung, R., and Gasteiger, H.A. (2018). Electrolyte and SEI Decomposition Reactions of Transition Metal Ions Investigated by On-Line Electrochemical Mass Spectrometry. Journal of The Electrochemical Society 165, A3304–A3312. 10.1149/2.0511814jes.

18. Björklund, E., Xu, C., Dose, W.M., Sole, C.G., Thakur, P.K., Lee, T.L., De Volder, M.F.L., Grey, C.P., and Weatherup, R.S. (2022). Cycle-Induced Interfacial Degradation and Transition-Metal Cross-Over in LiNi0.8Mn0.1Co0.1O2-Graphite Cells. Chemistry of Materials 34, 2034–2048. 10.1021/acs.chemmater.1c02722.

19. Prado, G., Suard, E., Fournes, L., and Delmas, C. (2000). Cationic distribution in the Li(1-z)(Ni(1-y)Fe(y))(1+z)O2 electrode materials. Journal of Materials Chemistry 10, 2553–2560. 10.1039/b002975k.

20. Croguennec, L., Suard, E., Willmann, P., and Delmas, C. (2002). Structural and electrochemical characterization of the LiNi1-yTiyO2 electrode materials obtained by direct solid-state reactions. Chemistry of Materials 14, 2149–2157. 10.1021/cm011265v.

21. Ober, S., Mesnier, A., and Manthiram, A. (2023). Surface Stabilization of Cobalt-Free LiNiO2with Niobium for Lithium-Ion Batteries. ACS Applied Materials and Interfaces. 10.1021/acsami.2c20268.

22. Cho, J., Kim, T.J., Kim, Y.J., and Park, B. (2001). High-performance ZrO2-coated LiNiO2 cathode material. Electrochemical and Solid-State Letters 4, 160–162. 10.1149/1.1398556.

23. Gao, Y., Park, J., and Liang, X. (2020). Comprehensive Study of Al- And Zr-Modified LiNi0.8Mn0.1Co0.1O2through Synergy of Coating and Doping. ACS Applied Energy

Materials 3, 8978–8987. 10.1021/acsaem.0c01420.

24. Lee, S.H., Park, G.J., Sim, S.J., Jin, B.S., and Kim, H.S. (2019). Improved electrochemical performances of LiNi0.8Co0.1Mn0.1O2 cathode via SiO2 coating. Journal of Alloys and Compounds 791, 193–199. 10.1016/j.jallcom.2019.03.308.

25. Kim, K., Ma, H., Park, S., and Choi, N.S. (2020). Electrolyte-Additive-Driven Interfacial Engineering for High-Capacity Electrodes in Lithium-Ion Batteries: Promise and Challenges. ACS Energy Letters 5, 1537–1553. 10.1021/acsenergylett.0c00468.

26. Yang, J., Liu, X., Wang, Y., Zhou, X., Weng, L., Liu, Y., Ren, Y., Zhao, C., Dahbi, M., Alami, J., et al. (2021). Electrolytes Polymerization-Induced Cathode-Electrolyte-Interphase for High Voltage Lithium-Ion Batteries. Advanced Energy Materials 11, 1–11. 10.1002/aenm.202101956.

27. Jang, S.H., Lee, K.J., Mun, J., Han, Y.K., and Yim, T. (2019). Chemically-induced cathode–electrolyte interphase created by lithium salt coating on Nickel-rich layered oxides cathode. Journal of Power Sources 410–411, 15–24. 10.1016/j.jpowsour.2018.11.008.

28. Wang, J., Yamada, Y., Sodeyama, K., Chiang, C.H., Tateyama, Y., and Yamada, A. (2016). Superconcentrated electrolytes for a high-voltage lithium-ion battery. Nature Communications 7, 1–9. 10.1038/ncomms12032.

29. Yamada, Y., Chiang, C.H., Sodeyama, K., Wang, J., Tateyama, Y., and Yamada, A. (2015). Corrosion Prevention Mechanism of Aluminum Metal in Superconcentrated Electrolytes. ChemElectroChem 2, 1687–1694. 10.1002/celc.201500235.

30. Qiao, L., Oteo, U., Martinez-Ibañez, M., Santiago, A., Cid, R., Sanchez-Diez, E., Lobato, E., Meabe, L., Armand, M., and Zhang, H. (2022). Stable non-corrosive sulfonimide salt for 4-V-class lithium metal batteries. Nature Materials 21, 455–462. 10.1038/s41563-021-01190-1.

31. Liu, W., Li, J., Li, W., Xu, H., Zhang, C., and Qiu, X. (2020). Inhibition of transition metals dissolution in cobalt-free cathode with ultrathin robust interphase in concentrated electrolyte. Nature Communications 11. 10.1038/s41467-020-17396-x.

32. Yamada, Y., Wang, J., Ko, S., Watanabe, E., and Yamada, A. (2019). Advances and issues in developing salt-concentrated battery electrolytes. Nature Energy 4, 269–280. 10.1038/s41560-019-0336-z.

33. T. Deng et al., *Joule*, **3**, 2550–2564 (2019) https://doi.org/10.1016/j.joule.2019.08.004.

34. Deng, T., Fan, X., Cao, L., Chen, J., Hou, S., Ji, X., Chen, L., Li, S., Zhou, X., Hu, E., et al. (2019). Designing In-Situ-Formed Interphases Enables Highly Reversible Cobalt-Free LiNiO2 Cathode for Li-ion and Li-metal Batteries. Joule 3, 2550–2564. 10.1016/j.joule.2019.08.004.

35. Hobold, G.M., Lopez, J., Guo, R., Minafra, N., Banerjee, A., Shirley Meng, Y., Shao-Horn, Y., and Gallant, B.M. (2021). Moving beyond 99.9% Coulombic efficiency for lithium anodes in liquid electrolytes. Nature Energy 6, 951–960. 10.1038/s41560-021-

00910-w.

36. Meunier, V., Souza, M.L. De, Morcrette, M., and Grimaud, A. (2022). Design of workflows for cross-talk detection and lifetime deviation onset in Li-ion batteries. Joule, 1–15. 10.1016/j.joule.2022.12.004.

37. M. S. Ding, (2003). Liquid Phase Boundaries, Dielectric Constant, and Viscosity of PC-DEC and PC-EC Binary Carbonates, *Journal of The Electrochemical Society*, **150**, A455, 10.1149/1.1557968

38. Atkins, D., Ayerbe, E., Benayad, A., Capone, F.G., Capria, E., Castelli, I.E., Cekic-Laskovic, I., Ciria, R., Dudy, L., Edström, K., et al. (2022). Understanding Battery Interfaces by Combined Characterization and Simulation Approaches: Challenges and Perspectives. Advanced Energy Materials 12. 10.1002/aenm.202102687.

39. Rueff, J.P., Rault, J.E., Ablett, J.M., Utsumi, Y., and Céolin, D. (2018). HAXPES for Materials Science at the GALAXIES Beamline. Synchrotron Radiation News 31, 4–9. 10.1080/08940886.2018.1483648.

40. Tanuma, S., Powell, C.J., and Penn, D.R. (2011). Calculations of electron inelastic mean free paths. IX. Data for 41 elemental solids over the 50 eV to 30 keV range. Surface and Interface Analysis 43, 689–713. 10.1002/sia.3522.

41. Dubouis, N., Marchandier, T., Rousse, G., Marchini, F., Fauth, F., Avdeev, M., Iadecola, A., Porcheron, B., Deschamps, M., Tarascon, J.M., et al. (2021). Extending insertion electrochemistry to soluble layered halides with superconcentrated electrolytes. Nature Materials 20, 1545–1550. 10.1038/s41563-021-01060-w.

42. Degoulange, D., Dubouis, N., and Grimaud, A. (2021). Toward the understanding of water-in-salt electrolytes: Individual ion activities and liquid junction potentials in highly concentrated aqueous solutions. Journal of Chemical Physics 155, 1–10. 10.1063/5.0058506.

43. Ruff, Z., Xu, C., and Grey, C.P. (2021). Transition Metal Dissolution and Degradation in NMC811-Graphite Electrochemical Cells. Journal of The Electrochemical Society 168, 060518. 10.1149/1945-7111/ac0359.

44. de Souza, M.L., Duquesnoy, M., Morcrette, M., and Franco, A.A. (2022). Electrochemistry Visualization Tool to Support the Electrochemical Analysis of Batteries. Batteries and Supercaps. 10.1002/batt.202200378.

45. Smith, A.J., Burns, J.C., and Dahn, J.R. (2011). High-precision differential capacity analysis of LiMn2O 4/graphite cells. Electrochemical and Solid-State Letters 14, 39–41. 10.1149/1.3543569.

46. Ansean, D., Garcia, V.M., Gonzalez, M., Blanco-Viejo, C., Viera, J.C., Pulido, Y.F., and Sanchez, L. (2019). Lithium-Ion Battery Degradation Indicators Via Incremental Capacity Analysis. IEEE Transactions on Industry Applications 55, 2992–3002. 10.1109/TIA.2019.2891213.

47. Birkl, C.R., Roberts, M.R., McTurk, E., Bruce, P.G., and Howey, D.A. (2017). Degradation diagnostics for lithium ion cells. Journal of Power Sources 341, 373–386.

10.1016/j.jpowsour.2016.12.011.

48. Xu, J., Deshpande, R.D., Pan, J., Cheng, Y.-T., and Battaglia, V.S. (2015). Electrode Side Reactions, Capacity Loss and Mechanical Degradation in Lithium-Ion Batteries. Journal of The Electrochemical Society 162, A2026–A2035. 10.1149/2.0291510jes.

49. Yan, G., Alves-Dalla-Corte, D., Yin, W., Madern, N., Gachot, G., and Tarascon, J.-M. (2018). Assessment of the Electrochemical Stability of Carbonate-Based Electrolytes in Na-Ion Batteries. Journal of The Electrochemical Society 165, A1222–A1230. 10.1149/2.0311807jes.

50. Yamada, Y., and Yamada, A. (2017). Superconcentrated electrolytes to create new interfacial chemistry in non-aqueous and aqueous rechargeable batteries. Chemistry Letters 46, 1056–1064. 10.1246/cl.170284.

51. Yamada, Y., Furukawa, K., Sodeyama, K., Kikuchi, K., Yaegashi, M., Tateyama, Y., and Yamada, A. (2014). Unusual stability of acetonitrile-based superconcentrated electrolytes for fast-charging lithium-ion batteries. Journal of the American Chemical Society 136, 5039–5046. 10.1021/ja412807w.

52. Klein, S., van Wickeren, S., Röser, S., Bärmann, P., Borzutzki, K., Heidrich, B., Börner, M., Winter, M., Placke, T., and Kasnatscheew, J. (2021). Understanding the Outstanding High-Voltage Performance of NCM523||Graphite Lithium Ion Cells after Elimination of Ethylene Carbonate Solvent from Conventional Electrolyte. Advanced Energy Materials 11. 10.1002/aenm.202003738.

53. Attia, P.M., Bills, A.A., Brosa Planella, F., Dechent, P., dos Reis, G., Dubarry, M., Gasper, P., Gilchrist, R., Greenbank, S., Howey, D., et al. (2022). Review—"Knees" in Lithium-Ion Battery Aging Trajectories. Journal of The Electrochemical Society, 1–93. 10.1149/1945-7111/ac6d13.

54. Waldmann, T., Wilka, M., Kasper, M., Fleischhammer, M., and Wohlfahrt-Mehrens, M. (2014). Temperature dependent ageing mechanisms in Lithium-ion batteries - A Post-Mortem study. Journal of Power Sources 262, 129–135. 10.1016/j.jpowsour.2014.03.112.

55. Yang, X.G., and Wang, C.Y. (2018). Understanding the trilemma of fast charging, energy density and cycle life of lithium-ion batteries. Journal of Power Sources 402, 489–498. 10.1016/j.jpowsour.2018.09.069.

56. Petzl, M., Kasper, M., and Danzer, M.A. (2015). Lithium plating in a commercial lithium-ion battery - A low-temperature aging study. Journal of Power Sources 275, 799–807. 10.1016/j.jpowsour.2014.11.065.

57. Dose, W.M., Xu, C., Grey, C.P., and De Volder, M.F.L. (2020). Effect of Anode Slippage on Cathode Cutoff Potential and Degradation Mechanisms in Ni-Rich Li-Ion Batteries. Cell Reports Physical Science 1, 100253. 10.1016/j.xcrp.2020.100253.

58. El Ouatani, L., Dedryvère, R., Siret, C., Biensan, P., Reynaud, S., Iratçabal, P., and Gonbeau, D. (2009). The Effect of Vinylene Carbonate Additive on Surface Film Formation on Both Electrodes in Li-Ion Batteries. Journal of The Electrochemical Society

156, A103. 10.1149/1.3029674.

59. Philippe, B., Dedryveìre, R., Gorgoi, M., Rensmo, H., Gonbeau, D., and Edström, K. (2013). Improved performances of nanosilicon electrodes using the salt LiFSI: A photoelectron spectroscopy study. Journal of the American Chemical Society 135, 9829–9842. 10.1021/ja403082s.

60. Dedryvère, R., Gireaud, L., Grugeon, S., Laruelle, S., Tarascon, J.M., and Gonbeau, D. (2005). Characterization of lithium alkyl carbonates by X-ray photoelectron spectroscopy: Experimental and theoretical study. Journal of Physical Chemistry B 109, 15868–15875. 10.1021/jp051626k.

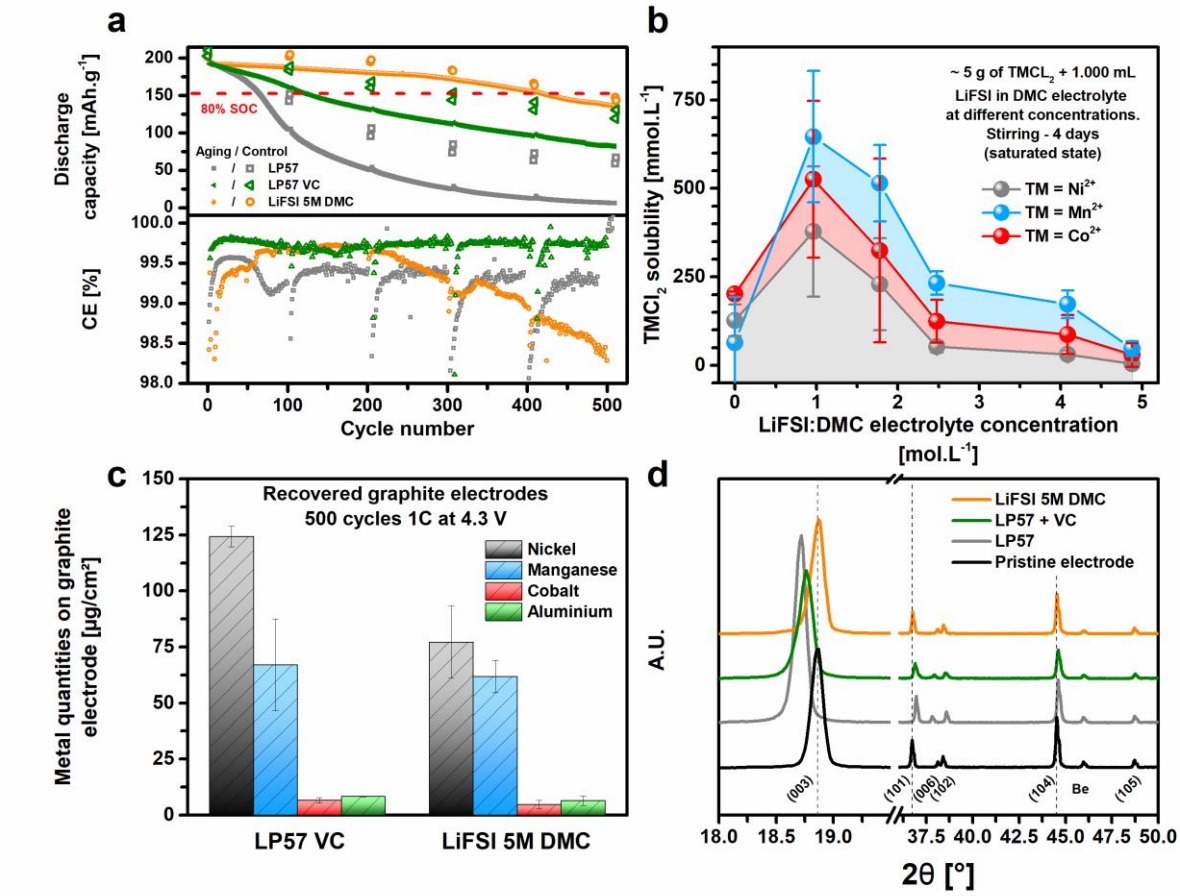

Figure 1: a) Cell performance recorded for graphite/NMC811 cells at 4.3 V - 25°C using LP57, LP57 VC and LiFSI 5M DMC. The control cycles are designated as follows: Control N corresponds to the cycle at C/20 that is measured after subjecting the battery to Nx100 aging cycles at 1C. b) Evolution of nickel, manganese and cobalt chloride salt solubilities in LiFSI:DMC electrolytes as a function of LiFSI concentration. c) Transition metal quantities measured on graphite electrodes retrieved after 500 cycles at 4.3 V using LP57 VC and LiFSI 5M DMC. Error bars are obtained from duplicated measurement. d) Post mortem X-ray diffractograms of NMC811 electrodes showing no early material fatigue after 500 cycles.

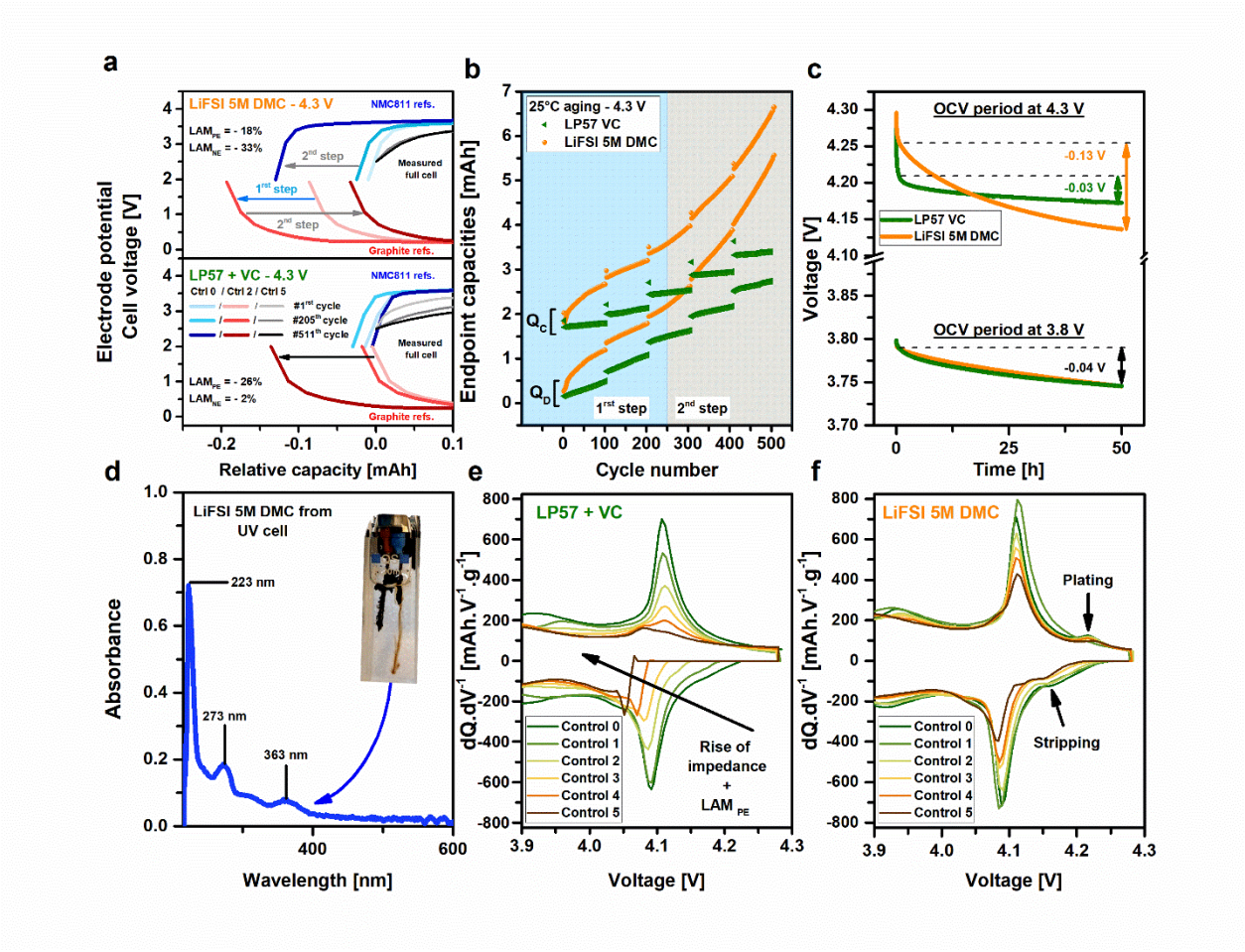

Figure 2: a) Derivative voltage analysis (DVA) of graphite/NMC811 cells cycled using LP57 VC and LiFSI 5M DMC. The control cycles are designated as follows: Control N corresponds to the cycle at C/20 that is measured after subjecting the battery to Nx100 aging cycles at 1C. b) Associated marching capacities. c) Self discharge tests at 3.8 V and 4.3 V. d) UV-visible spectrum of the species released at the positive electrode when using LiFSI 5M DMC electrolyte. Incremental capacity analysis (ICA) performed on C/20 control cycle for LP57 VC e) and HCE-DMC f).

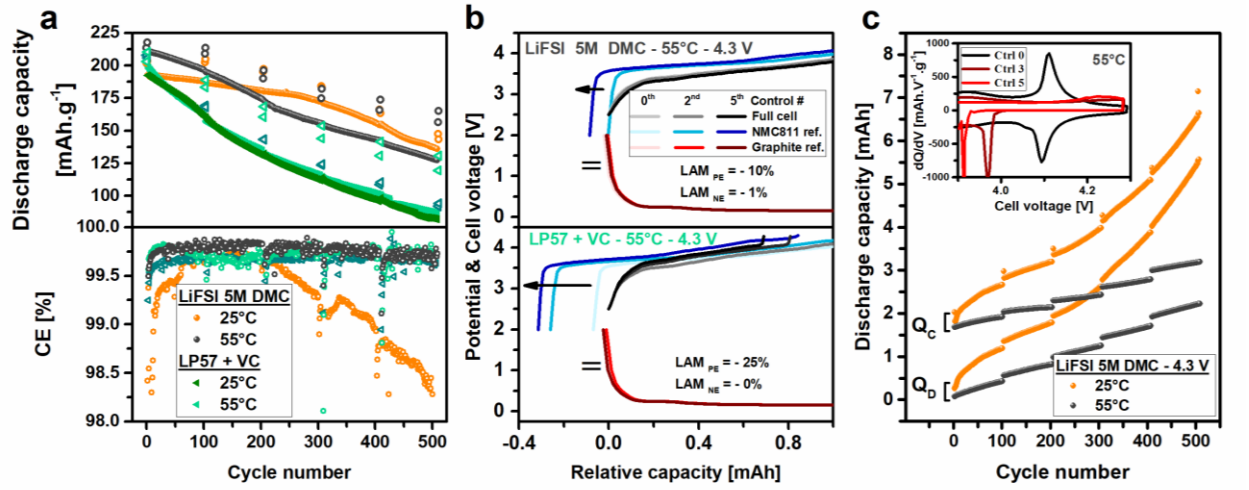

Figure 3: a) Graphite/NMC811 performance at 55°C – 4.3 V for cells cycled using LP57 VC and LiFSI 5M DMC electrolyte. b) Associated derivative voltage analysis. c) Capacity endpoints of LiFSI 5M DMC at 25°C and 55°C. Incremental capacity analysis for cell cycled in LiFSI 5M DMC at 55°C is given in insert. The control cycles are designated as follows: Control N corresponds to the cycle at C/20 that is measured after subjecting the battery to Nx100 aging cycles at 1C.

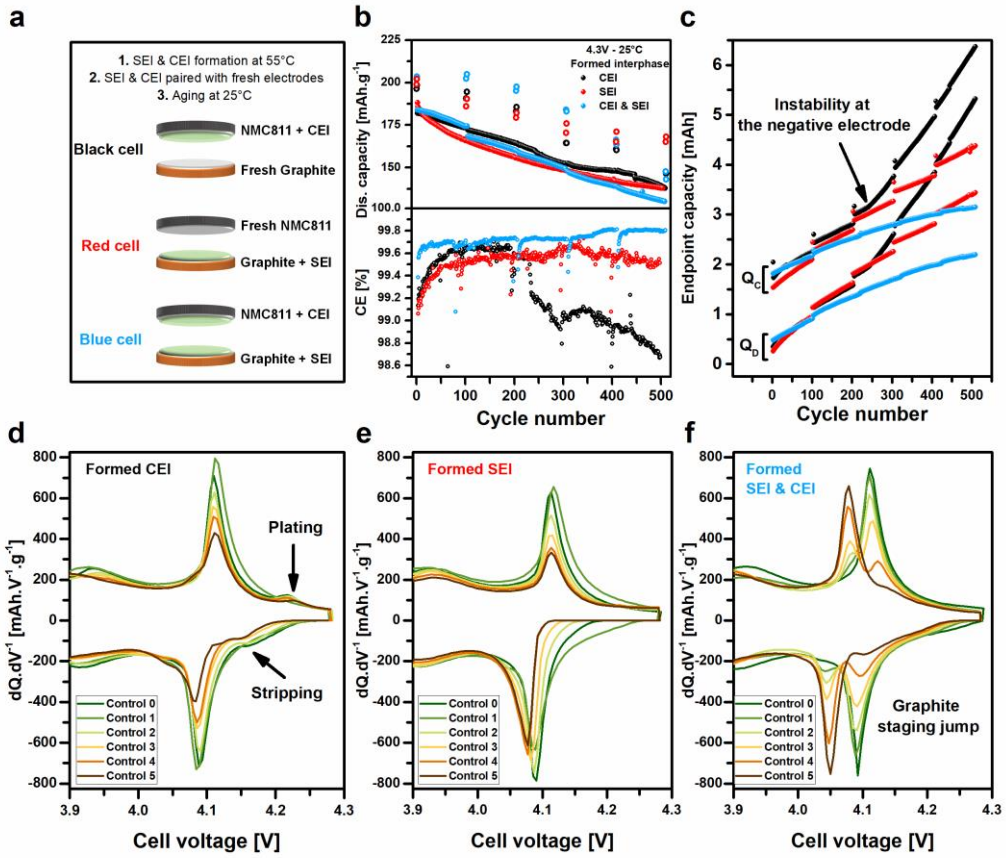

Figure 4: a) Schematic view of the interphases pre-formation steps performed at 55°C and tested conditions. b) Cycling performance of reassembled cells with the interphases pre-formed at 55°C. c) Shift of capacity endpoints recorded for cells using pre-formed interphases. Incremental capacity analysis of cells which CEI d), SEI e) and both CEI and SEI are pre-formed at 55°C. The control cycles are designated as follows: Control N corresponds to the cycle at C/20 that is measured after subjecting the battery to Nx100 aging cycles at 1C.

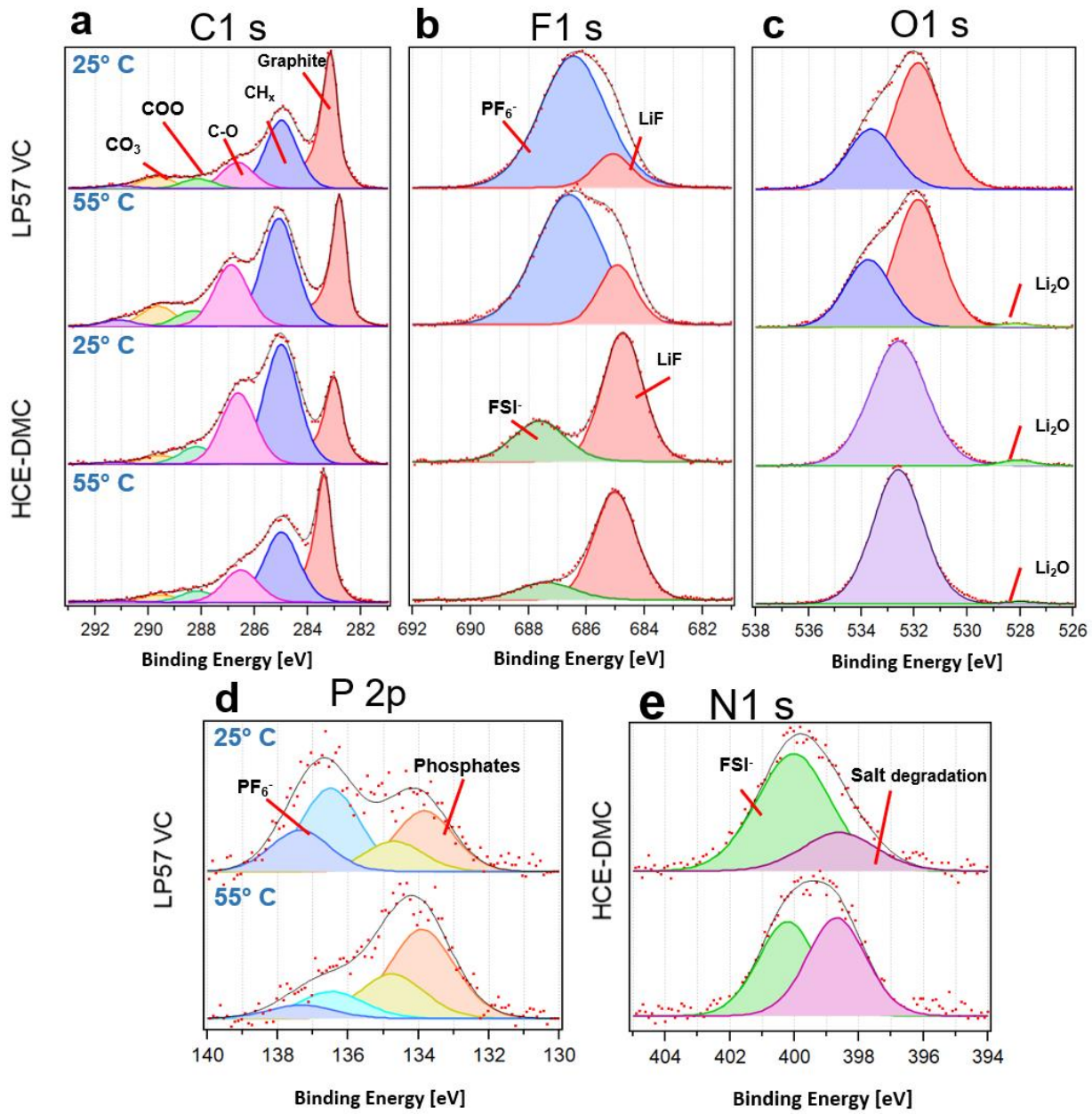

Figure 5: a), C 1s, b) F 1s and c) O 1s HAXPES spectra of graphite electrodes recovered from graphite/NMC811 cells after 100 cycles performed at 25 and 55°C, using LP57 VC and LiFSI 5M DMC electrolytes. d) P 2p spectra in the case of LP57 VC ($LiPF_6$ salt), and e) N 1s spectra in the case of LiFSI 5M DMC. The HAXPES spectra were recorded with 3 keV photon energy.

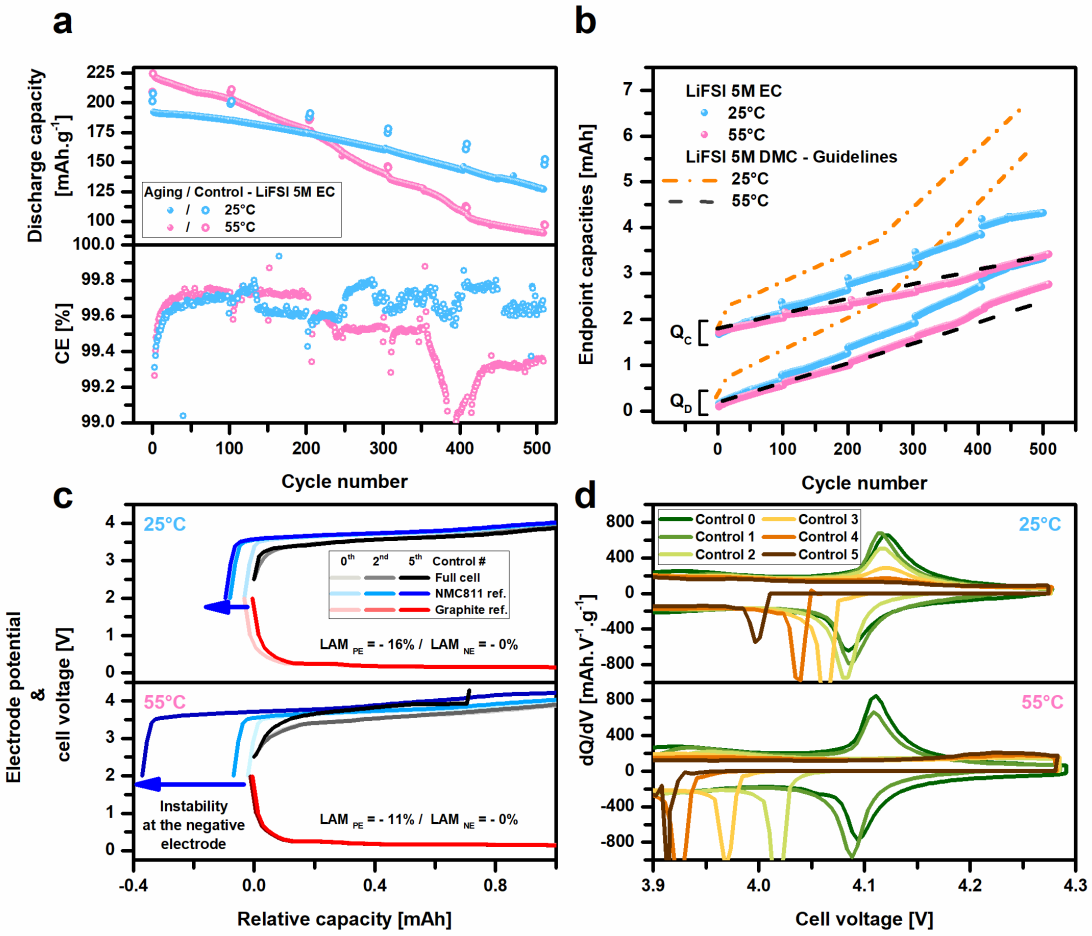

Figure 6: a) Cycling performance measured using LiFSI 5M EC at 25 and 55°C. The control cycles are designated as follows: Control N corresponds to the cycle at C/20 that is measured after subjecting the battery to Nx100 aging cycles at 1C. b) Comparison of marching capacities between LiFSI 5M DMC and LiFSI 5M EC as a function of cycling temperature. c) DVA of the cells using HCE-EC at 25°C (higher panel) and 55°C (lower panel). d) ICA performed at 25°C (upper panel) and 55°C (low panel) for HCE-EC.